Medical Image Analysis 83 (2023) 102674

Contents lists available at ScienceDirect

Medical Image Analysis

journal homepage: www.elsevier.com/locate/media

Signed graph representation learning for functional-to-structural brain network mapping

Haoteng Tang [a,*], Lei Guo [a], Xiyao Fu [a], Yalin Wang [d], Scott Mackin [e], Olusola Ajilore [c], Alex D. Leow [c], Paul M. Thompson [b], Heng Huang [a], Liang Zhan [a,*]

[a] University of Pittsburgh, 3700 O'Hara St., Pittsburgh, 15261, PA, USA
[b] University of Southern California, 2001 N. Soto St., Los Angeles, 90032, CA, USA
[c] University of Illinois Chicago, 1601 W. Taylor St., Chicago, 60612, IL, USA
[d] Arizona State University, 699 S Mill Ave., Tempe, 85281, AZ, USA
[e] University of California San Francisco, 505 Parnassus Ave., San Francisco, 94143, CA, USA

ARTICLE INFO

Keywords:
Signed graph learning
Multimodal
Structural network
Functional network
Reconstruction
Prediction

ABSTRACT

MRI-derived brain networks have been widely used to understand functional and structural interactions among brain regions, and factors that affect them, such as brain development and diseases. Graph mining on brain networks can facilitate the discovery of novel biomarkers for clinical phenotypes and neurodegenerative diseases. Since brain functional and structural networks describe the brain topology from different perspectives, exploring a representation that combines these cross-modality brain networks has significant clinical implications. Most current studies aim to extract a fused representation by projecting the structural network to the functional counterpart. Since the functional network is dynamic and the structural network is static, mapping a static object to a dynamic object may not be optimal. However, mapping in the opposite direction (i.e., from functional to structural networks) are suffered from the challenges introduced by negative links within signed graphs. Here, we propose a novel graph learning framework, named as Deep Signed Brain Graph Mining or DSBGM, with a signed graph encoder that, from an opposite perspective, learns the cross-modality representations by projecting the functional network to the structural counterpart. We validate our framework on clinical phenotype and neurodegenerative disease prediction tasks using two independent, publicly available datasets (HCP and OASIS). Our experimental results clearly demonstrate the advantages of our model compared to several state-of-the-art methods.

1. Introduction

Recent years have witnessed great progress in applying graph theory to study MRI-derived brain networks, to discover novel biomarkers for clinical phenotypes or neurodegenerative diseases (e.g., Alzheimer's disease or AD) (Hao et al., 2013; Uludağ and Roebroeck, 2014; Calhoun and Sui, 2016; Rusinek et al., 2003). Different MRI techniques can be used to reconstruct brain networks corresponding to different aspects of the brain organization or dynamics (Qi et al., 2015; Wierenga et al., 2016; Fornito et al., 2016). For example, functional MRI-derived functional networks provide measures of BOLD signals' relationships over time between brain regions but cannot guarantee the existence of physical neuronal links among those regions (Bathelt et al., 2013; Fischer et al., 2014). By contrast, diffusion MRI-derived structural network describes white matter tracts between brain regions, yet does not inform us about whether this tract, or the regions it connects, are "activated" or "not activated" in a specific state (Sotiropoulos and Zalesky, 2019; Yeh et al., 2021; Soares et al., 2013; Tang et al., 2022a). Therefore, different types of brain networks provide distinct but complementary information, and separately analyzing each of these networks may be suboptimal.

Graph neural networks (GNNs) (Kipf and Welling, 2016a; Veličković et al., 2017) have gained enormous attentions recently. Although many progresses (Kawahara et al., 2017; Ktena et al., 2018; Sserwadda and Rekik, 2021; Zhang et al., 2020b; Bessadok et al., 2019b,a; Zhang and Huang, 2019; Yan et al., 2019; Tang et al., 2021) have been made by applying GNNs to brain networks, most existing techniques are developed based on single-modality brain networks. It is well known that a high-level dependency, based on network communications, exists between brain structural and functional networks (Ajilore et al., 2013; Rusinek et al., 2003; Bullmore and Sporns, 2012; Korthauer et al., 2018; Calamante, 2017; Ge et al., 2013; Lv et al., 2010, 2011; Huang et al.,

* Corresponding authors.
E-mail addresses: haoteng.tang@pitt.edu (H. Tang), liang.zhan@pitt.edu (L. Zhan).

https://doi.org/10.1016/j.media.2022.102674
Received 20 June 2022; Received in revised form 4 October 2022; Accepted 27 October 2022
Available online 17 November 2022

2019), which has motivated many studies (Zhang et al., 2020b; Huang and Ding, 2016; Finger et al., 2016; Zhu et al., 2021; Dsouza et al., 2021; Zhang et al., 2021) to integrate multimodal brain networks by constructing a projection between them using GNNs (e.g., Zhang et al., 2020b). However, most existing studies aim to reconstruct functional networks from brain structural counterparts (Zhang et al., 2020b; Bao et al., 2020; Huang and Ding, 2016; Finger et al., 2016). Mapping a static object (i.e., structural network) to a dynamic one (i.e., functional network) may not be an optimal solution since the static object is better served as the template. Very few studies have been conducted for the opposite mapping (i.e., from functional to structural networks), which mainly due to that current GNNs focus on unsigned graphs (i.e., structural networks in which all edge weights are non-negative) while brain functional network is a signed graph by definition (including entries that denote negative correlations); as such, these negative network edges may undermine the mechanism of information aggregation in current GNNs (Derr et al., 2018). Some pioneering studies (e.g., Zhang et al., 2022, 2020a) convert signed functional networks to non-negative networks using absolute or threshold operations and successfully applied GNNs to embed those non-negative functional networks to reconstruct structural networks. However, those negative edges contains important information to explore the dynamics in brain functional networks and several studies have demonstrated the possibility that negative edges are related to large-scale modulation and inhibition (Liang et al., 2012; Gopinath et al., 2015; Zhan et al., 2017; Conrin et al., 2018; Derr et al., 2018; Gu et al., 2019; Fortel et al., 2020; Tang et al., 2022b). Therefore, these negative edges are of significant biological meanings and removing them will completely alter brain functional network's topological structure, which leads to suboptimal outcomes. We demonstrate this in Section 5.5.

To tackle this, we propose a new framework to encode the signed graphs, and apply this framework to encode brain functional networks to corresponding structural networks. Our results on two publicly available data demonstrate that the extracted latent network representations from our model can be used for different clinical tasks (regression and classification) with better performances, compared with baseline methods. Our contributions are three-fold:

- We propose an end-to-end network representation learning framework to model brain structural networks from brain functional networks.
- We propose a signed graph encoder to embed the functional brain networks.
- We draw graph saliency maps for clinical tasks, to enable phenotypic and disease-related biomarker detection and aid in the biological interpretation.

2. Data description and preprocessing

Two publicly available datasets were used to evaluate our framework. The first includes data from 1206 young healthy subjects (mean age 28.19 ± 7.15, 657 women) from the Human Connectome Project (Van Essen et al., 2013) (HCP). The second includes 1326 subjects (mean age $= 70.42 \pm 8.95$, 738 women) from the Open Access Series of Imaging Studies (OASIS) dataset (LaMontagne et al., 2019). Details of each dataset may be found on their official websites.[1][2] Functional network was reconstructed using the standard pipeline in CONN toolbox (Whitfield-Gabrieli and Nieto-Castanon, 2012). In brief, raw EPI images were realigned, co-registered, normalized, and smoothed before analyses. Confound effects from motion artifact, white matter, and CSF were regressed out of the signal. Functional networks were then defined using Pearson Correlations of BOLD sequences between pair of ROIs. Structural network was reconstructed using FSL Probtrackx and Bedpostx functions (Behrens et al., 2007). In our study, up to three fibers were modeled per voxel. We chose all voxels with $FA \geq 0.2$ as the seeds. Probtrackx was run on each individual seed voxel and repeatedly samples from the voxel-wise principal diffusion directions. This builds a distribution on the likely tract location and path, given the data. 1000 iterations were run to ensure convergence of the Markov chains, from which the posterior distributions of the local estimate of the fiber orientation distribution were sampled. For the HCP data, both networks have a dimension of 82×82 based on Destrieux atlas (Destrieux et al., 2010). For the OASIS data, both networks have a dimension of 132×132 based on the Harvard-Oxford Atlas (Desikan et al., 2006) and AAL Atlas (Tzourio-Mazoyer et al., 2002). We deliberately chose different network resolutions for HCP and OASIS, to evaluate whether the performance of our new framework is affected by the network dimension or atlas. Both network reconstruction procedures have been comprehensively verified in our previous studies (Zhan et al., 2015; Korthauer et al., 2018).

3. Preliminaries of signed brain networks

A brain network is an attributed and weighted graph $G = \{V, E\} = (A, X)$ with N nodes, where $V = \{v_i\}_{i=1}^{N}$ is the set of graph nodes representing brain regions, and $E = \{e_{i,j}\}$ is the edge set. $X \in \mathcal{R}^{N \times d}$ is the node feature matrix where $x_i \in \mathbb{R}^{1 \times d}$ is the $i-$th row of X representing the node feature of v_i. $A \in \mathbb{R}^{N \times N}$ is the adjacency matrix where $a_{i,j} \in \mathbb{R}$ represents the weights of the edge between v_i and v_j. In signed brain networks (i.e., brain functional networks), $a_{i,j} \in (-\infty, +\infty)$, while in unsigned brain networks (i.e., brain structural networks), $a_{i,j} \in [0, +\infty)$. We use $G^F = (A^F, X^F)$ and $G^S = (A^S, X^S)$ to represent brain functional and structural networks, respectively. Given a specific node v_i in a signed network, we define their positive and negative neighbors set as $\mathcal{N}_i^+$ and $\mathcal{N}_i^-$, respectively. Following the balance theory (Cartwright and Harary, 1956; Derr et al., 2018; Heider, 1946; Li et al., 2020), any node v_j belongs to the balanced set (denoted as $\mathbf{\Gamma}$) of v_i if the path between v_i and v_i contains even number of negative edges. Otherwise, v_j belongs to the unbalanced set (denoted as $\mathbf{\Upsilon}$) of v_i.

4. Methodology

In this section, we first introduce the proposed multi-head signed graph encoder (SGE). Then, we present an end-to-end framework with the proposed encoder to reconstruct structural networks from functional networks and perform downstream tasks.

4.1. Signed graph encoder (SGE)

Our SGE consists of a balanced–unbalanced encoder (BUE) head and a positive–negative encoder (PNE) head. Motivated by the balance theory in Section 3, the BUE head encodes the graph node to the latent features with balanced and unbalanced components. Meanwhile, we split the signed graph into a positive sub-graph and a negative counterpart. The PNE head encodes these two sub-graphs to generate the node latent features with positive and negative components. The yellow and blue boxes in Fig. 1 illustrate the BUE and PNE, respectively.

4.1.1. Balanced-unbalanced encoder (BUE)

We use T to denote the encoder layer number and the $T-th$ layer of the encoder focuses on aggregating the $T-th$ hop neighbors of node v_i.[3] To improve the generalization of local information aggregation in brain networks, a dynamic and fluctuating adjustment of aggregation weights (i.e., brain network edge weights) is arguably more reasonable

[1] https://www.oasis-brains.org
[2] https://wiki.humanconnectome.org

[3] Hop is a jump describing the node connection in graph. To a target node v_i, $T-th$ hop neighbors are the nodes connected to v_i via a path with T edges.

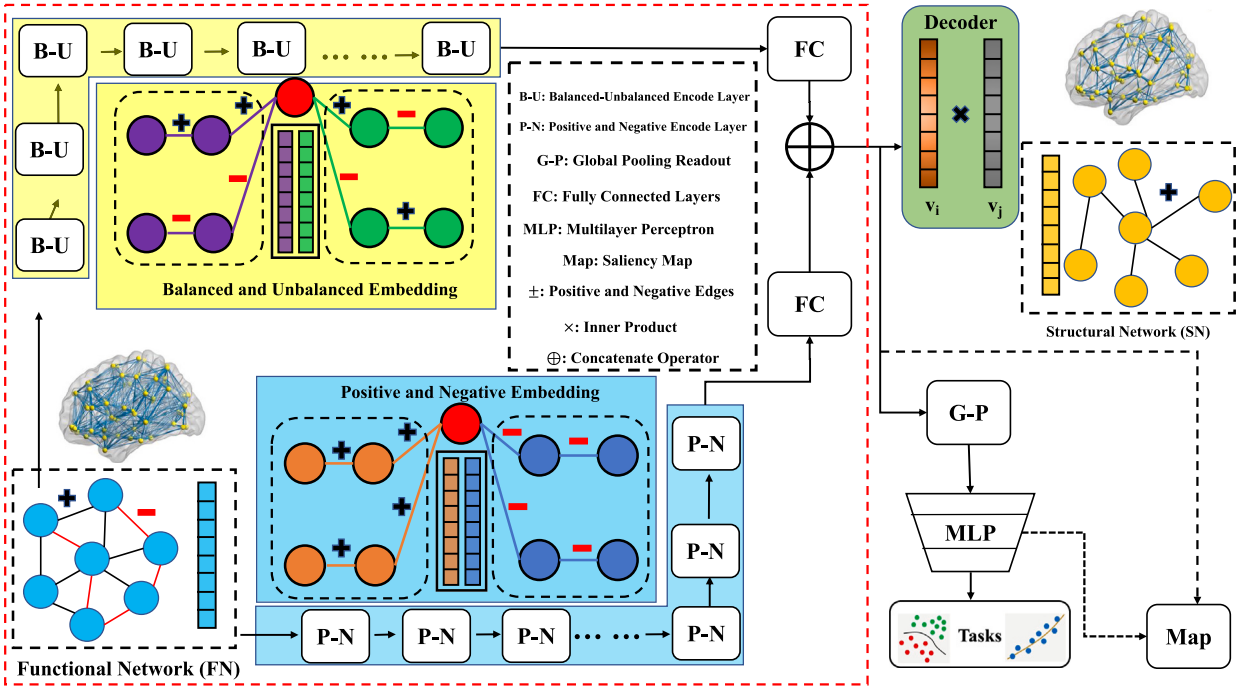

Fig. 1. Pipeline of the DSBGM framework, including a signed graph encoder (in red dash blox) scheme with two branches (BUE and PNE encoder heads in yellow and blue box) for functional network embedding, an inner-product decoder for structural network reconstruction and a downstream task branch for classification and regression.

and has been advocated during graph learning (Zhang et al., 2020b). To this end, our BUE is designed based on the concept of graph attention (Veličković et al., 2017).

Initial Layer ($T = 1$). We initialize balanced and unbalanced node latent feature components by:

$$x_i^{\Gamma(1)} = \sigma\Big(\sum_{j\in\mathcal{N}_i^+} \alpha_{i,j}^{\Gamma(1)} x_j^{(0)} W^{\Gamma(1)}\Big), \quad x_i^{\Upsilon(1)} = \sigma\Big(\sum_{j\in\mathcal{N}_i^-} \alpha_{i,j}^{\Upsilon(1)} x_j^{(0)} W^{\Upsilon(1)}\Big), \tag{1}$$

where σ is a nonlinear activation function (i.e., $\sigma = ReLU(\cdot)$). We use $x_i^{(0)}$ to denote the input feature of node v_i for the first layer and $x_i^{(0)}$ is initialized by the graph original node features, x_i. $W^{\Gamma(1)}$ and $W^{\Upsilon(1)}$ are trainable weights to generate two latent feature components. $\alpha_{i,j}^{\Gamma(1)}$ and $\alpha_{i,j}^{\Upsilon(1)}$ are attention scores of brain nodes from the balanced and unbalanced set respectively. Following the work in Veličković et al. (2017), we first compute the attention coefficients by:

$$e_{i,j}^{\Gamma(1)} = a[x_i^{(0)} W^{\Gamma(1)}, x_j^{(0)} W^{\Gamma(1)}], \quad e_{i,j}^{\Upsilon(1)} = a[x_i^{(0)} W^{\Upsilon(1)}, x_j^{(0)} W^{\Upsilon(1)}] \tag{2}$$

where a is a trainable attentional weight vector and $[,]$ is a concatenation operator. Based on the attention coefficients, we derive the attention scores by:

$$\alpha_{i,j}^{\Gamma(1)} = \frac{exp(e_{i,j}^{\Gamma(1)})}{\sum_{n\in\mathcal{N}_i^+} exp(e_{i,n}^{\Gamma(1)})}, \quad \alpha_{i,j}^{\Upsilon(1)} = \frac{exp(e_{i,j}^{\Upsilon(1)})}{\sum_{n\in\mathcal{N}_i^-} exp(e_{i,n}^{\Upsilon(1)})} \tag{3}$$

Following Layers ($T > 1$). In the subsequent layers ($T > 1$), $x_i^{\Gamma(T)}$ and $x_i^{\Upsilon(T)}$ is generated by:

$$\begin{aligned} x_i^{\Gamma(T)} &= \sigma\Big(\sum_{j\in\mathcal{N}_i^+, k\in\mathcal{N}_i^-} \alpha_{i,j}^{\Gamma(T)} x_j^{\Gamma(T-1)} W^{\Gamma(T)} + \alpha_{i,k}^{\Gamma(T-1)} x_k^{\Upsilon(T-1)} W^{\Gamma(T)}\Big) \\ x_i^{\Upsilon(T)} &= \sigma\Big(\sum_{j\in\mathcal{N}_i^+, k\in\mathcal{N}_i^-} \alpha_{i,j}^{\Upsilon(T)} x_j^{\Upsilon(T-1)} W^{\Upsilon(T)} + \alpha_{i,k}^{\Upsilon(T-1)} x_k^{\Gamma(T-1)} W^{\Upsilon(T)}\Big) \end{aligned} \tag{4}$$

where $\sigma = ReLU(\cdot)$. Similarly, we compute 4 attention coefficients as

$$\begin{aligned} e_{i,j}^{\Gamma(T)} &= a[x_i^{\Gamma(T-1)} W^{\Gamma(T)}, x_j^{\Gamma(T-1)} W^{\Gamma(T)}] \\ e_{i,k}^{\Gamma(T)} &= a[x_i^{\Upsilon(T-1)} W^{\Gamma(T)}, x_k^{\Upsilon(T-1)} W^{\Gamma(T)}] \\ e_{i,j}^{\Upsilon(T)} &= a[x_i^{\Upsilon(T-1)} W^{\Upsilon(T)}, x_j^{\Upsilon(T-1)} W^{\Upsilon(T)}] \\ e_{i,k}^{\Upsilon(T)} &= a[x_i^{\Gamma(T-1)} W^{\Upsilon(T)}, x_k^{\Gamma(T-1)} W^{\Upsilon(T)}] \end{aligned} \tag{5}$$

Based on these 4 attention coefficients, we compute 4 attention scores by:

$$\begin{aligned} \alpha_{i,j}^{\Gamma(T)} &= \frac{exp(e_{i,j}^{\Gamma(T)})}{\sum_{\Gamma(T)}}, \quad \alpha_{i,k}^{\Gamma(T)} = \frac{exp(e_{i,k}^{\Gamma(T)})}{\sum_{\Gamma(T)}}, \\ \alpha_{i,j}^{\Upsilon(T)} &= \frac{exp(e_{i,j}^{\Upsilon(T)})}{\sum_{\Upsilon(T)}}, \quad \alpha_{i,k}^{\Upsilon(T)} = \frac{exp(e_{i,k}^{\Upsilon(T)})}{\sum_{\Upsilon(T)}} \end{aligned} \tag{6}$$

After we obtain the two latent components, we concatenate them as the latent features generated by the BUE head by: $x_i^{BUE} = [x_i^{\Gamma}, x_i^{\Upsilon}]$.

4.1.2. Positive-negative encoder (PNE)

We split the adjacency matrix of the functional network into positive and negative sub-network pairs (i.e., $G^{+F} = (A^{+F}, X)$ and $G^{-F} = (A^{-F}, X)$). For each sub-network, we forward it into T graph attention layers (Veličković et al., 2017) to generate the positive and negative latent feature components (i.e., x_i^+ and x_i^-). As a result, the latent feature generated by the PNE head can be computed by $x_i^{PNE} = [x_i^+, x_i^-]$. The final fused latent features generated by our SGE can be computed by: $x_i = [x_i^{BUE} W, x_i^{PNE} W]$, where W is a set of trainable parameters to control feature dimensions.

4.2. Deep signed brain networks model (DSBGM)

Our DSBGM framework is illustrated in Fig. 1, which includes (1) a signed graph encoder (SGE) to generate the latent node features from brain functional networks, (2) a decoder to reconstruct brain structural networks from latent node features, and (3) Multilayer Perceptrons (MLP) for downstream tasks.

4.2.1. Structural network reconstruction and downstream tasks

The structural network edges can be reconstructed by an inner-product decoder (Kipf and Welling, 2016b) as: $\hat{a}_{i,j}^S = sigmoid(x_i^\top \cdot x_j)$, where the $\cdot$ is an inner-product operator, $\top$ is vector transpose.

We use a sum function as a global readout operator to obtain the whole graph representation (i.e., $X_G = \sum_{i=1}^N x_i$). Then, MLP are

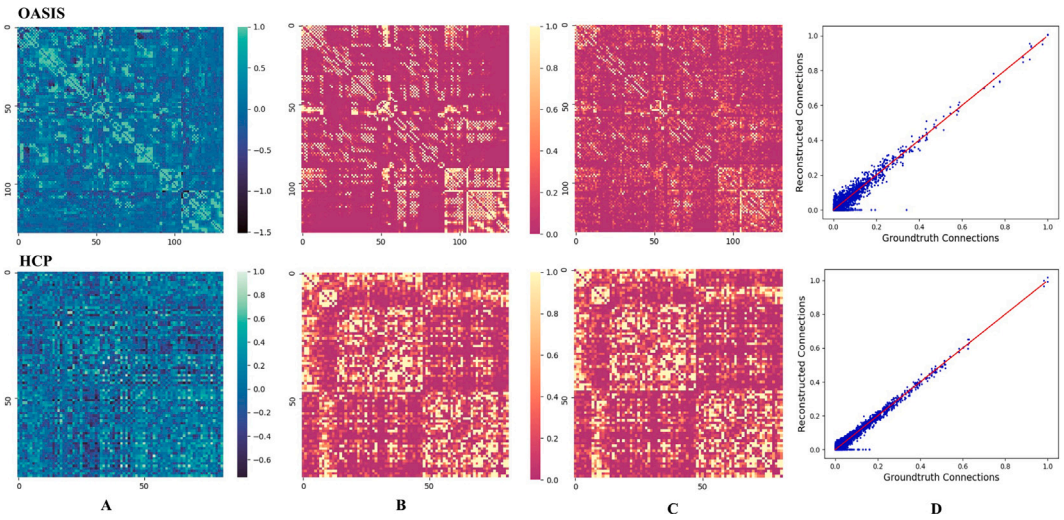

Fig. 2. Cross-modality learning results on the OASIS and HCP data. **(A)** are the averaged functional networks, **(B)** and **(C)** are the mean reconstructed and ground-truth structural networks. **(D)** demonstrate that edge weights in the predicted structural network are significantly correlated with the ground truth data ($r = 0.917$ with $p = 0.0129$ for OASIS data, and $r = 0.945$ with $p = 0.0086$ for HCP data.).

used to generate the final classification or regression output (i.e., $\hat{y} = MLP(X_G)$). Moreover, we use parameters in the last MLP layer and node latent features x_i to generate the brain network saliency map using the Class Activation Mapping (CAM) approach (Pope et al., 2019; Arslan et al., 2018) for the classification task. Particularly, assume that the fused latent feature x_i generated by SGE is in the dimension of $\mathcal{R}^{1\times D}$, and the parameters in the last MLP layer (i.e., W_{MLP}) are in the dimension of $\mathcal{R}^{D\times C}$ where C is the output dimension. The saliency value for node v_i with respect to each class is computed by: $x_i \cdot W_{MLP}$ which is in the dimension of $\mathcal{R}^{1\times C}$. We compute a saliency value for each brain node (i.e., v_i for $i \in \{1, 2, \ldots, N\}$) with respect to each class to generate a saliency map for the whole brain network. The generated saliency map highlights important brain regions based on saliency values for each class.

4.2.2. Loss functions

We summarize the loss functions here for our framework.

Reconstruction Loss. The ground-truth brain structural network is sparse while the reconstructed structural network is fully connected. To facilitate network reconstruction, in the training stage, we add a small perturbation value (δ) to the edge weights of the ground-truth structural networks (i.e., $\bar{a}^S_{i,j} = a^S_{i,j} + \delta$) and build up the reconstruction loss as $\mathcal{L}_{recon} = \frac{1}{|E|}\sum_{i,j}(\hat{a}^S_{i,j} - \bar{a}^S_{i,j})^2$, where $|E|$ is the number of edges.

Supervised Loss. We deploy our framework on both regression and classification tasks. For the classification task, we use the negative log likelihood loss where $\mathcal{L}_{super} = NLLLoss(\hat{y}, y)$. For the regression task, we use L_1 loss where $\mathcal{L}_{super} = L_1Loss(\hat{y}, y)$. In summary, the overall loss function of the DSBGM is $\mathcal{L}_{all} = \eta_1\mathcal{L}_{recon} + \eta_2\mathcal{L}_{super}$, where η_1, η_2 are loss weights.

5. Experiments

5.1. Implementation details

The edge weights of the functional networks and structural networks were first normalized to the range of $[-1, 1]$ and $[0, 1]$, respectively. The node features are initialized as the min, 25%, median, 75%, max values of the mean fMRI bold signal in that node (or brain region). We randomly split each dataset into 5 disjoint sets for 5-fold cross-validations in the following experiments. The model is trained using the Adam optimizer with a batch size of 128. The initial learning rate is set to 0.001 and decayed by $(1 - \frac{current\ epoch}{max\ epoch})^{0.9}$. We also regularize the training with an L_2 weight decay of $1e^{-5}$. We stop the training if the validation loss does not improve for 100 epochs in an epoch termination condition with a maximum of 500 epochs, as was done in Lee et al. (2019), Shchur et al. (2018). The experiments are deployed on NVIDIA TITAN RTX GPU.

5.2. Brain structural network reconstruction using DSBGM

To show the performance of our DSBGM on the reconstruction of brain structural networks, we train the model in a task-free manner where no task-specific supervised loss is involved. Since the δ value is set to 0.05 when we train the model, we set the reconstructed edge weights to 0 if the predicted weights are less than 0.05. The mean absolute error (MAE) values between the edge weights in the ground-truth and reconstructed networks are 0.074 ± 0.016 and 0.039 ± 0.058 under 5-fold cross-validation on the OASIS and HCP data, respectively. The reconstruction results on OASIS data are visualized in Fig. 2 and the correlation between the predicted structural network and ground truth is 0.917 with p value $= 0.0129$.

5.3. Disease and sex classification tasks

Experimental Setup. 7 baseline methods were used for comparison. The baseline methods include 2 traditional graph embedding models (i.e., t-BNE (Cao et al., 2017) and MK-SVM (Dyrba et al., 2015)), 2 deep graph convolution models designed for brain network embedding (i.e., BrainChey (Ktena et al., 2018) and BrainNet-CNN (Kawahara et al., 2017)) and 2 hierarchical graph neural networks with graph pooling strategies (i.e., DIFFPOOL (Ying et al., 2018) and SAGPOOL (Lee et al., 2019)). We also introduce variational graph auto-encoders (VGAE) (Kipf and Welling, 2016b) with GCN as graph encoders to our baseline methods to integrate multimodal brain networks by reconstructing the structural networks from functional networks.

As mentioned above, baseline methods can only embed unsigned graphs, we therefore adopt two different strategies to convert signed functional networks to unsigned networks as the input of baseline methods. On the one hand, we compute the absolute values of the functional network edge weights; on the other hand, we only preserve positive edges and drop negative ones to yield unsigned networks. 3 variant models of our DSBGM, including DSBGM w/o BUE encoder, DSBGM w/o PNE encoder and DSBGM w/o reconstruction decoder, are evaluated for ablation studies. The number of BUE and PNE encoder layers is set to 3. We search the loss weights (see details in Fig. 3) η_1 and η_2 in the range of $[0.01, 0.1, 0.5, 1]$ and $[0.1, 1, 5]$ respectively, and

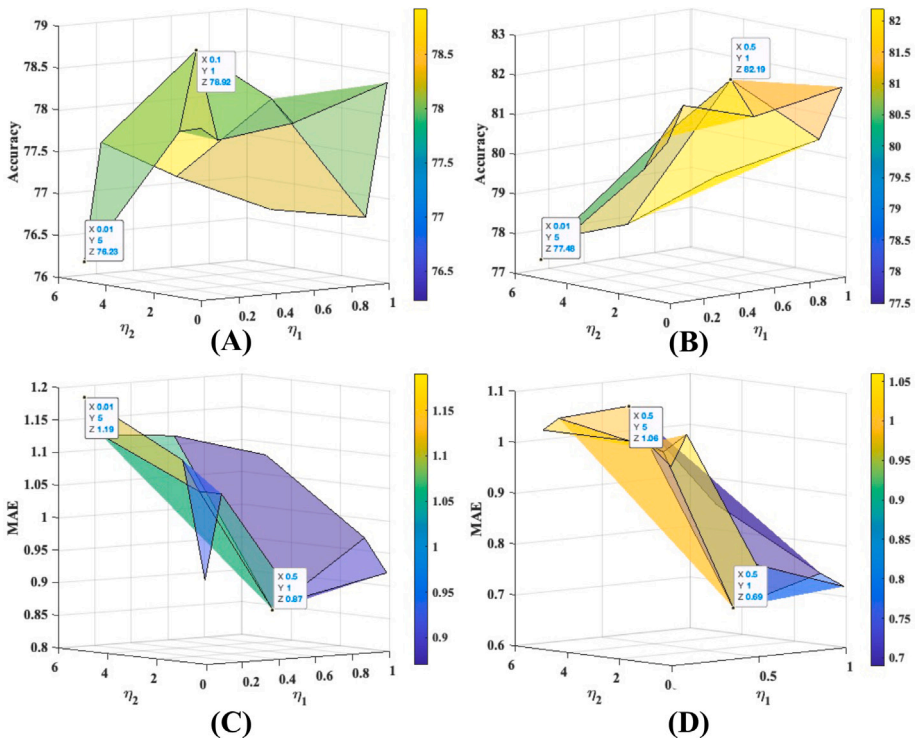

Fig. 3. Loss weights analysis. For the AD classification **(A)**, the best $\eta_1 = 0.5, \eta_2 = 1$. For the gender classification **(B)**, the best $\eta_1 = 0.1, \eta_2 = 1$. For the MMSE regression on OASIS **(C)** and HCP **(D)** data, the best $\eta_1 = 0.5, \eta_2 = 1$.

Table 1a
Classification accuracy, precision, and F1-scores, with their standard deviation values under 5-fold cross-validation. Signed functional networks are converted to unsigned networks as inputs of all baseline methods by computing the absolute values of the edge weights. The best results are highlighted in **bold** font.

Method	OASIS (Disease)			HCP (Gender)		
	Acc.	Prec.	F1	Acc.	Prec.	F1
t-BNE	57.84 ± 2.14	52.26 ± 2.39	55.17 ± 3.15	59.84 ± 2.05	57.77 ± 2.21	55.89 ± 1.96
MK-SVM	54.62 ± 3.33	49.86 ± 3.11	55.27 ± 4.15	58.21 ± 3.75	51.51 ± 2.84	59.19 ± 2.40
DIFFPOOL	66.29 ± 2.60	63.87 ± 2.14	69.91 ± 2.37	72.12 ± 1.81	68.84 ± 1.97	74.01 ± 2.16
SAGPOOL	64.53 ± 2.06	61.76 ± 2.99	68.97 ± 3.07	69.29 ± 1.84	70.18 ± 1.49	67.38 ± 1.12
BrainChey	69.26 ± 1.47	71.22 ± 1.95	70.46 ± 2.81	74.11 ± 2.05	76.26 ± 1.77	75.08 ± 2.60
BrainNet-CNN	73.37 ± 2.14	74.06 ± 1.59	73.27 ± 1.85	71.88 ± 1.69	70.18 ± 2.21	70.29 ± 2.10
VGAE	72.11 ± 2.66	70.08 ± 1.30	71.55 ± 0.96	73.59 ± 2.44	73.43 ± 1.80	72.77 ± 1.03
DSBGM w/o BUE	73.04 ± 3.03	74.74 ± 1.96	73.53 ± 2.23	78.15 ± 2.96	79.01 ± 1.68	80.47 ± 2.02
DSBGM w/o PNE	75.38 ± 2.52	76.26 ± 2.96	78.68 ± 3.02	80.78 ± 2.44	81.16 ± 1.74	82.98 ± 2.01
DSBGM w/o Recon.	75.94 ± 2.73	77.09 ± 2.52	75.46 ± 2.17	79.12 ± 2.06	80.55 ± 2.18	81.19 ± 1.96
DSBGM	**78.92 ± 1.38**	**79.81 ± 1.41**	**80.22 ± 2.25**	**82.19 ± 2.01**	**85.35 ± 1.99**	**84.71 ± 2.37**

determine the loss weights as $\eta_1 = 0.1$, $\eta_2 = 1$ for AD classification, $\eta_1 = 0.1$, $\eta_2 = 1$ for sex classification. The results are reported in terms of classification accuracy, precision and F1-scores, with their *std*.

Results. Classification results for AD on OASIS and sex on HCP are summarized in Table 1a and 1b, where Table 1a presents the results with the absolute edge weights as inputs of baseline methods and Table 1b presents the results with the positive-only edges as inputs of baseline methods. These results demonstrate that our model achieves the best accuracy, comparing with all baseline methods using two different input settings, on both classification tasks. For example, in the AD classification, our model outperforms baselines with at least 7.6%, 7.8% and 9.4% increases in accuracy, precision and F1 scores respectively when using absolute edge weights as inputs of baseline methods. And it outperforms baselines with at least 8.47%, 11.90% and 11.08% increases in accuracy, precision and F1 scores respectively when using positive-only edges as inputs of baseline methods. Either computing absolute edge weights or dropping negative edges leads to an information deficiency of signed functional networks, which may partially account for performance decreases on baseline methods. Moreover, results from baseline methods with two input strategies are not consistent. For example, using absolute edge weights outperforms using only-positive edges for DIFFPOOL on gender classification, however, using only-positive edges is better for SAGPOOL on the same task. Therefore, no recommendation can be made between these two input strategies for baseline methods. In general, deep graph models perform better than traditional graph embedding methods (i.e., t-BNE and MK-SVM). When we abandon the cross-modality learning (i.e., DSBGM w/o Recon.), the performance, though comparable to baselines, decreases significantly. This shows the effectiveness of the cross-modality learning. The performance will also decrease when we remove BUE encoder or PNE encoder, which indicates that both balance and polarity properties are essential for embedding signed graphs (e.g., functional

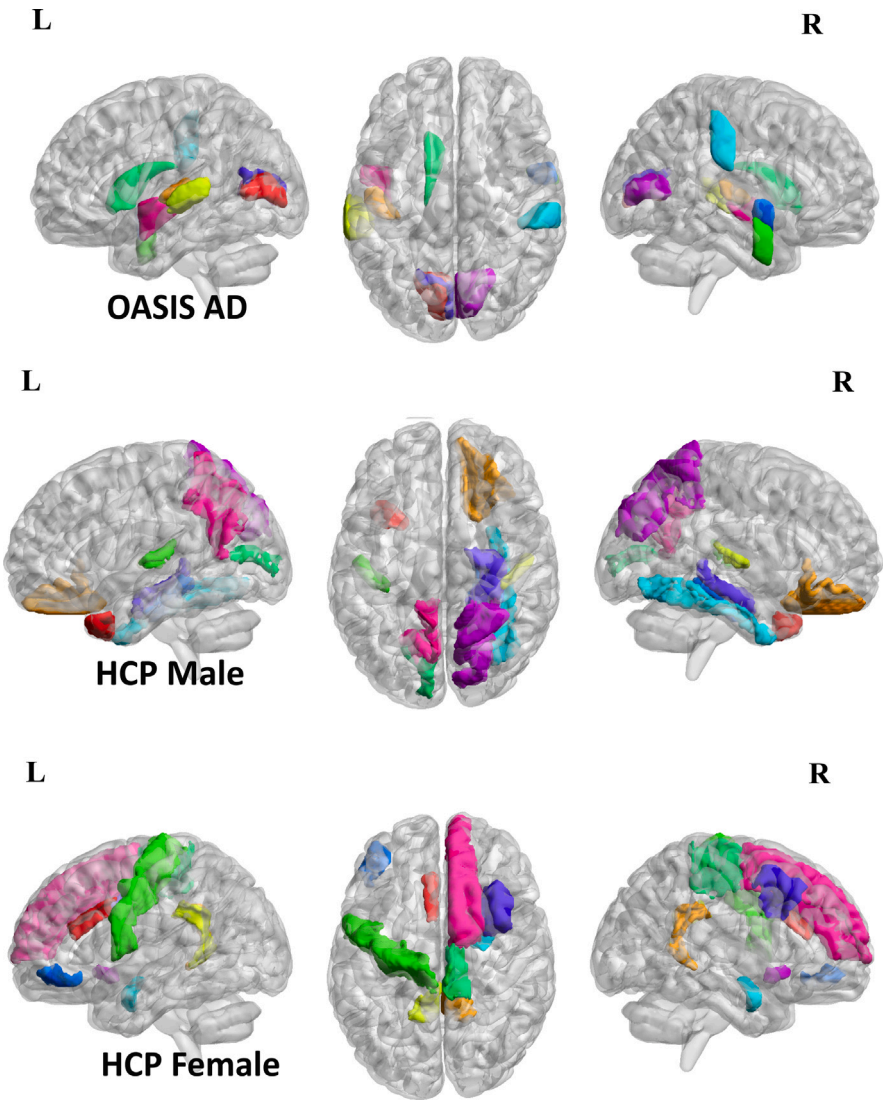

Fig. 4. Saliency maps to identify top 10 regions associated with AD (from OASIS) and with each sex (from HCP), respectively.

Table 1b
Classification accuracy, precision, and F1-scores, with their standard deviation values under 5-fold cross-validation. Signed functional networks are converted to unsigned networks as inputs of all baseline methods by dropping all negative edges. The best results are highlighted in **bold** font.

Method	OASIS (Disease)			HCP (Gender)		
	Acc.	Prec.	F1	Acc.	Prec.	F1
t-BNE	56.26 ± 2.98	56.03 ± 2.48	57.71 ± 2.41	61.26 ± 1.91	60.17 ± 2.49	62.29 ± 3.57
MK-SVM	55.29 ± 3.02	50.34 ± 2.83	57.27 ± 1.73	57.97 ± 3.78	53.12 ± 2.31	58.82 ± 2.82
DIFFPOOL	68.97 ± 1.34	66.03 ± 3.36	69.24 ± 1.83	67.77 ± 3.56	65.25 ± 2.65	68.82 ± 1.72
SAGPOOL	65.65 ± 2.01	63.33 ± 1.95	67.27 ± 2.09	70.95 ± 2.88	69.83 ± 1.85	71.44 ± 1.29
BrainChey	72.76 ± 2.20	71.27 ± 2.58	72.21 ± 3.55	75.01 ± 1.82	75.70 ± 1.51	74.22 ± 2.72
BrainNet-CNN	69.54 ± 2.97	70.03 ± 1.24	68.22 ± 1.40	70.92 ± 1.79	70.41 ± 2.19	71.11 ± 1.71
VGAE	64.68 ± 2.49	62.57 ± 2.19	65.85 ± 1.91	73.59 ± 2.42	74.43 ± 1.84	76.25 ± 1.49
DSBGM w/o BUE	73.04 ± 3.03	74.74 ± 1.96	73.53 ± 2.23	78.15 ± 2.96	79.01 ± 1.68	80.47 ± 2.02
DSBGM w/o PNE	75.38 ± 2.52	76.26 ± 2.96	78.68 ± 3.02	80.78 ± 2.44	81.16 ± 1.74	82.98 ± 2.01
DSBGM w/o Recon.	75.94 ± 2.73	77.09 ± 2.52	75.46 ± 2.17	79.12 ± 2.06	80.55 ± 2.18	81.19 ± 1.96
DSBGM	**78.92 ± 1.38**	**79.81 ± 1.41**	**80.22 ± 2.25**	**82.19 ± 2.01**	**85.35 ± 1.99**	**84.71 ± 2.37**

brain networks). Although VGAE and our DSBGM integrate multimodal brain networks in a reconstruction manner, our model takes signed functional networks as the input while VGAE can only take unsigned ones as the input. Our model outperforms VGAE in both classification tasks. This suggests that negative edges contain important information for network's topological structure, which is essential for network representation learning. Ignoring or removing these negative edges may lead to significant information loss. The same conclusion is also demonstrated in regression tasks in next section.

The brain saliency map is shown in Fig. 4 where 10 key brain regions associated with AD (from OASIS data) and with each sex (from HCP data) are identified, respectively. The salient regions for females

Table 2a
Regression Mean Absolute Error (MAE) ± *std* under 5-fold cross-validation. Signed functional networks are converted to unsigned networks as the input of all baseline methods by computing the absolute values of the edge weights. Lower MAE values indicate better results. The best results are highlighted in **bold** font.

	OASIS (MMSE) ↓	HCP (MMSE) ↓
tBNE	2.39 ± 0.74	2.17 ± 0.48
SAGPOOL	1.86 ± 0.27	1.55 ± 0.33
DIFFPOOL	1.69 ± 0.36	1.63 ± 0.14
BrainNet-CNN	1.40 ± 0.20	1.29 ± 0.06
BrainChey	1.12 ± 0.19	1.14 ± 0.25
VGAE	1.27 ± 0.25	1.31 ± 0.20
DSBGM w/o BUE	1.17 ± 0.22	1.11 ± 0.17
DSBGM w/o PNE	1.06 ± 0.24	0.86 ± 0.34
DSBGM w/o Recon.	0.97 ± 0.11	1.03 ± 0.19
DSBGM	$\mathbf{0.87 \pm 0.18}$	$\mathbf{0.69 \pm 0.21}$

Table 2b
Regression Mean Absolute Error (MAE) ± *std* under 5-fold cross-validation. Signed functional networks are converted to unsigned networks as the input of all baseline methods by dropping all negative edges. Lower MAE values indicate better results. The best results are highlighted in **bold** font.

	OASIS (MMSE) ↓	HCP (MMSE) ↓
tBNE	2.51 ± 0.21	2.02 ± 0.93
SAGPOOL	1.73 ± 0.79	1.46 ± 0.29
DIFFPOOL	1.77 ± 0.56	1.39 ± 0.15
BrainNet-CNN	1.39 ± 0.42	1.44 ± 0.09
BrainChey	1.19 ± 0.67	1.06 ± 0.49
VGAE	1.11 ± 0.16	1.21 ± 0.28
DSBGM w/o BUE	1.17 ± 0.22	1.11 ± 0.17
DSBGM w/o PNE	1.06 ± 0.24	0.86 ± 0.34
DSBGM w/o Recon.	0.97 ± 0.11	1.03 ± 0.19
DSBGM	$\mathbf{0.87 \pm 0.18}$	$\mathbf{0.69 \pm 0.21}$

are concentrated in frontal regions of the brain while males have a different trend, consistent with the finding in (Carlo et al., 1999) that women are typically less aggressive than men, and, on average, less physically strong. For AD, most of the salient regions are located in subcortical structures, as well as the bilateral intracalcarine region, the caudate, and planum polare, which have been implicated as potential AD biomarkers in the literature (Amoroso et al., 2017). The name of these brain regions are summarized in Table 3

5.4. MMSE regression

Experimental Setup. Mini-Mental State Exam (MMSE) is a quantitative measure of cognitive status in adults. In the MMSE regression task, the selected baselines for comparison (except for MK-SVM which is designed only for classification problems) and the structure of our DSBGM remain unchanged. The loss weights are set to $\eta_1 = 0.5$ and $\eta_2 = 1$ for both datasets. Details of hyperparameter analysis are provided in Fig. 3. The regression results are reported as average Mean Absolute Errors (MAE) with their *std*.

Results. MMSE regression results on the HCP and OASIS data are summarized in Table 2a and 2b, where Table 2a presents the results with the absolute edge weights as inputs for baseline methods and Table 2b presents the results with the positive-only edges as inputs for baseline methods. Our results show that the DSBGM outperforms all baselines using any of two input settings. And this clearly demonstrates the same three conclusions as those in classification tasks in the above section, which are (1) the superiority of the cross-modality learning; (2) the essential of negative edges in the signed graph (i.e., brain functional network); and (3) the importance of both BUE and PNE encoders. Moreover, our results indicate that the regression performance on HCP dataset is better than on OASIS dataset, which may be attributed to the range of original data (i.e., data *std*). The original mean ± *std* of MMSE are 28.38 ± 2.84 and 28.99 ± 2.26 for OASIS and HCP, respectively. And a lower deviation value of original data may result in a more precise regression result.

5.5. Group analysis on B-U set and P-N set

To further demonstrate that the balanced–unbalanced (B-U) node sets and positive–negative (P-N) node sets are important signed graph topological structures, we compare these two node sets between disease groups (i.e., AD vs. NC groups) on OASIS dataset. Specifically, we search B-U sets and P-N sets on functional brain networks and compute two ratios (r_{B-U} and r_{P-N}) for each subject.

$$r_{B-U} = \frac{\#\ of\ B\ sets}{\#\ of\ U\ sets}, \quad r_{P-N} = \frac{\#\ of\ P\ sets}{\#\ of\ N\ sets}. \tag{7}$$

r_{B-U} value will change with the order (i.e., 1st, 2nd and 3rd order) so that each subject will have multiple r_{B-U} values. While for P-N sets, only the 1st order is meaningful and there is no higher order for P-N sets, so there is only one r_{P-N} value for each subject.

We conduct student t test on these r_{B-U} and r_{P-N} values between AD and NC groups. The p values of B-U sets in 1st, 2nd and 3rd order are 3.2×10^{-4}, 6.9×10^{-5} and 2.7×10^{-5}, respectively. The p value of the 1st order P-N set is 3.2×10^{-4}. These results suggest that there exist significant groups differences in both balanced–unbalanced node sets and positive–negative node sets, and these node sets are important topological features to distinguish the patterns of functional networks.

6. Conclusion

We propose a novel multimodal brain network representation learning framework with a signed functional network encoder. The cross-modality network embedding is generated by mapping a functional brain network to its structural counterpart. Our results indicate negative edges are essential for graph topological representation learning, which is consistent with the literature (Zhan et al., 2017). Moreover, we showed that BUE and PNE encoders are both necessary for the signed graph learning. The embedded network representations contribute to important clinical prediction tasks and the brain saliency map may assist with disease-related biomarker identification. We will explore the bijection mapping between these two brain networks in the future.

Declaration of competing interest

The authors declare that they have no known competing financial interests or personal relationships that could have appeared to influence the work reported in this paper.

Data availability

The authors do not have permission to share data.

Acknowledgments

This study is partially supported by The National Institutes of Health, USA (R01AG071243, R01MH125928 and U01AG068057) and National Science Foundation, USA (IIS 2045848 and IIS 1837956).

Data were provided [in part] by the Human Connectome Project, MGH-USC Consortium (Principal Investigators: Bruce R. Rosen, Arthur W. Toga and Van Wedeen; U01MH093765) funded by the NIH Blueprint Initiative for Neuroscience Research grant; the National Institutes of Health, USA grant P41EB015896, and the Instrumentation Grants S10RR023043, 1S10RR023401, 1S10RR019307.

Data were provided [in part] by OASIS-3: Longitudinal Multimodal Neuroimaging: Principal Investigators: T. Benzinger, D. Marcus, J. Morris; NIH P30 AG066444, P50 AG00561, P30 NS09857781, P01 AG026276, P01 AG003991, R01 AG043434, UL1 TR000448, R01 EB009352. AV-45 doses were provided by Avid Radiopharmaceuticals, a wholly owned subsidiary of Eli Lilly.

Part of the work used the Extreme Science and Engineering Discovery Environment (XSEDE), which is supported by National Science Foundation, USA grant number ACI-1548562. Specifically, it used the Bridges system, which is supported by NSF award number ACI-1445606, at the Pittsburgh Supercomputing Center (PSC).

Table 3
The names of top 10 brain regions in the saliency map.

HCP		OASIS
Female	Male	AD
R-Superior frontal cortex	L-Precuneus	L-Planum Polare
R-Accumbens-area	R-Superior parietal cortex	R-Intracalcarine Cortex
R-Caudal middle frontal cortex	R-Hippocampus	L-Supracalcarine Cortex
L-Parsorbitalis	R-Parahippocampal	R-Superior Temporal Gyrus, anterior division
R-Amygdala	R-fusiform cortex	R-Supramarginal Gyrus, anterior division
R-Paracentral cortex	L-Pericalcarine	L-Caudate
L-Precentral cortex	L-transverse temporal cortex	R-Middle Temporal Gyrus, anterior division
L-isthmus cingulate	R-transverse temporal cortex	L-Superior Temporal Gyrus, posterior division
R-isthmus cingulate	R-Lateral orbitofrontal	L-Heschl's Gyrus
L-Caudal anterior cingulate	L-Temporal pole	L-Intracalcarine Cortex

References

Ajilore, O., Zhan, L., GadElkarim, J., Zhang, A., Feusner, J.D., Yang, S., Thompson, P.M., Kumar, A., Leow, A., 2013. Constructing the resting state structural connectome. Front. Neuroinform. 7, 30.

Amoroso, N., La Rocca, M., Bruno, S., Maggipinto, T., Monaco, A., Bellotti, R., Tangaro, S., 2017. Brain structural connectivity atrophy in alzheimer's disease. arXiv preprint arXiv:1709.02369.

Arslan, S., Ktena, S.I., Glocker, B., Rueckert, D., 2018. Graph saliency maps through spectral convolutional networks: Application to sex classification with brain connectivity. In: Graphs in Biomedical Image Analysis and Integrating Medical Imaging and Non-Imaging Modalities. Springer, pp. 3–13.

Bao, R., Gu, B., Huang, H., 2020. Fast OSCAR and OWL regression via safe screening rules. In: International Conference on Machine Learning. PMLR, pp. 653–663.

Bathelt, J., O'Reilly, H., Clayden, J.D., Cross, J.H., de Haan, M., 2013. Functional brain network organisation of children between 2 and 5 years derived from reconstructed activity of cortical sources of high-density eeg recordings. NeuroImage 82, 595–604.

Behrens, T.E., Berg, H.J., Jbabdi, S., Rushworth, M.F., Woolrich, M.W., 2007. Probabilistic diffusion tractography with multiple fibre orientations: What can we gain? Neuroimage 34 (1), 144–155.

Bessadok, A., Mahjoub, M.A., Rekik, I., 2019a. Hierarchical adversarial connectomic domain alignment for target brain graph prediction and classification from a source graph. In: International Workshop on PRedictive Intelligence in MEdicine. Springer, pp. 105–114.

Bessadok, A., Mahjoub, M.A., Rekik, I., 2019b. Symmetric dual adversarial connectomic domain alignment for predicting isomorphic brain graph from a baseline graph. In: International Conference on Medical Image Computing and Computer-Assisted Intervention. Springer, pp. 465–474.

Bullmore, E., Sporns, O., 2012. The economy of brain network organization. Nat. Rev. Neurosci. 13 (5), 336–349.

Calamante, F., 2017. Track-weighted imaging methods: extracting information from a streamlines tractogram. Magn. Reson. Mater. Phys. Biol. Med. 30 (4), 317–335.

Calhoun, V.D., Sui, J., 2016. Multimodal fusion of brain imaging data: a key to finding the missing link (s) in complex mental illness. Biol. Psychiatry: Cognit. Neurosci. Neuroimaging 1 (3), 230–244.

Cao, B., He, L., Wei, X., Xing, M., Yu, P.S., Klumpp, H., Leow, A.D., 2017. T-bne: Tensor-based brain network embedding. In: Proceedings of the 2017 SIAM International Conference on Data Mining. SIAM, pp. 189–197.

Carlo, G., Raffaelli, M., Laible, D.J., Meyer, K.A., 1999. Why are girls less physically aggressive than boys? Personality and parenting mediators of physical aggression. Sex Roles 40 (9), 711–729.

Cartwright, D., Harary, F., 1956. Structural balance: a generalization of Heider's theory. Psychol. Rev. 63 (5), 277.

Conrin, S.D., Zhan, L., Morrissey, Z.D., Xing, M., Forbes, A., Maki, P., Milad, M.R., Ajilore, O., Langenecker, S.A., Leow, A.D., 2018. From default mode network to the basal configuration: sex differences in the resting-state brain connectivity as a function of age and their clinical correlates. Front. Psychiatry 9, 365.

Derr, T., Ma, Y., Tang, J., 2018. Signed graph convolutional networks. In: 2018 IEEE International Conference on Data Mining. ICDM, IEEE, pp. 929–934.

Desikan, R.S., Ségonne, F., Fischl, B., Quinn, B.T., Dickerson, B.C., Blacker, D., Buckner, R.L., Dale, A.M., Maguire, R.P., Hyman, B.T., et al., 2006. An automated labeling system for subdividing the human cerebral cortex on MRI scans into gyral based regions of interest. Neuroimage 31 (3), 968–980.

Destrieux, C., Fischl, B., Dale, A., Halgren, E., 2010. Automatic parcellation of human cortical gyri and sulci using standard anatomical nomenclature. Neuroimage 53 (1), 1–15.

Dsouza, N.S., Nebel, M.B., Crocetti, D., Robinson, J., Mostofsky, S., Venkataraman, A., 2021. M-gcn: A multimodal graph convolutional network to integrate functional and structural connectomics data to predict multidimensional phenotypic characterizations. In: Medical Imaging with Deep Learning. PMLR, pp. 119–130.

Dyrba, M., Grothe, M., Kirste, T., Teipel, S.J., 2015. Multimodal analysis of functional and structural disconnection in a lzheimer's disease using multiple kernel SVM. Human Brain Mapp. 36 (6), 2118–2131.

Finger, H., Bönstrup, M., Cheng, B., Messé, A., Hilgetag, C., Thomalla, G., Gerloff, C., König, P., 2016. Modeling of large-scale functional brain networks based on structural connectivity from DTI: comparison with EEG derived phase coupling networks and evaluation of alternative methods along the modeling path. PLoS Comput. Biol. 12 (8), e1005025.

Fischer, F.U., Wolf, D., Scheurich, A., Fellgiebel, A., 2014. Association of structural global brain network properties with intelligence in normal aging. PLoS One 9 (1), e86258.

Fornito, A., Zalesky, A., Bullmore, E., 2016. Fundamentals of Brain Network Analysis. Academic Press.

Fortel, I., Korthauer, L.E., Morrissey, Z., Zhan, L., Ajilore, O., Wolfson, O., Driscoll, I., Schonfeld, D., Leow, A., 2020. Connectome signatures of hyperexcitation in cognitively intact middle-aged female APOE-ε4 carriers. Cerebral Cortex 30 (12), 6350–6362.

Ge, B., Guo, L., Zhang, T., Hu, X., Han, J., Liu, T., 2013. Resting state fMRI-guided fiber clustering: methods and applications. Neuroinformatics 11 (1), 119–133.

Gopinath, K., Krishnamurthy, V., Cabanban, R., Crosson, B.A., 2015. Hubs of anticorrelation in high-resolution resting-state functional connectivity network architecture. Brain Connect. 5 (5), 267–275.

Gu, H., Hu, Y., Chen, X., He, Y., Yang, Y., 2019. Regional excitation-inhibition balance predicts default-mode network deactivation via functional connectivity. Neuroimage 185, 388–397.

Hao, X., Xu, D., Bansal, R., Dong, Z., Liu, J., Wang, Z., Kangarlu, A., Liu, F., Duan, Y., Shova, S., et al., 2013. Multimodal magnetic resonance imaging: The coordinated use of multiple, mutually informative probes to understand brain structure and function. Human Brain Mapp. 34 (2), 253–271.

Heider, F., 1946. Attitudes and cognitive organization. J. Psychol. 21 (1), 107–112.

Huang, H., Ding, M., 2016. Linking functional connectivity and structural connectivity quantitatively: a comparison of methods. Brain Connect. 6 (2), 99–108.

Huang, J., Zhou, L., Wang, L., Zhang, D., 2019. Integrating functional and structural connectivities via diffusion-convolution-bilinear neural network. In: International Conference on Medical Image Computing and Computer-Assisted Intervention. Springer, pp. 691–699.

Kawahara, J., Brown, C.J., Miller, S.P., Booth, B.G., Chau, V., Grunau, R.E., Zwicker, J.G., Hamarneh, G., 2017. BrainNetCNN: Convolutional neural networks for brain networks; towards predicting neurodevelopment. NeuroImage 146, 1038–1049.

Kipf, T.N., Welling, M., 2016a. Semi-supervised classification with graph convolutional networks. arXiv preprint arXiv:1609.02907.

Kipf, T.N., Welling, M., 2016b. Variational graph auto-encoders. arXiv preprint arXiv:1611.07308.

Korthauer, L.E., Zhan, L., Ajilore, O., Leow, A., Driscoll, I., 2018. Disrupted topology of the resting state structural connectome in middle-aged APOE ϵ4 carriers. Neuroimage 178, 295–305.

Ktena, S.I., Parisot, S., Ferrante, E., Rajchl, M., Lee, M., Glocker, B., Rueckert, D., 2018. Metric learning with spectral graph convolutions on brain connectivity networks. NeuroImage 169, 431–442.

LaMontagne, P.J., Benzinger, T.L., Morris, J.C., Keefe, S., Hornbeck, R., Xiong, C., Grant, E., Hassenstab, J., Moulder, K., Vlassenko, A.G., et al., 2019. OASIS-3: longitudinal neuroimaging, clinical, and cognitive dataset for normal aging and alzheimer disease. MedRxiv.

Lee, J., Lee, I., Kang, J., 2019. Self-attention graph pooling. In: International Conference on Machine Learning. PMLR, pp. 3734–3743.

Li, Y., Tian, Y., Zhang, J., Chang, Y., 2020. Learning signed network embedding via graph attention. In: Proceedings of the AAAI Conference on Artificial Intelligence. Vol. 34, (04), pp. 4772–4779.

Liang, Z., King, J., Zhang, N., 2012. Anticorrelated resting-state functional connectivity in awake rat brain. Neuroimage 59 (2), 1190–1199.

Lv, J., Guo, L., Hu, X., Zhang, T., Li, K., Zhang, D., Yang, J., Liu, T., 2010. Fiber-centered analysis of brain connectivities using DTI and resting state FMRI data. In: International Conference on Medical Image Computing and Computer-Assisted Intervention. Springer, pp. 143–150.

Lv, J., Guo, L., Li, K., Hu, X., Zhu, D., Han, J., Liu, T., 2011. Activated fibers: fiber-centered activation detection in task-based FMRI. In: Biennial International Conference on Information Processing in Medical Imaging. Springer, pp. 574–587.

Pope, P.E., Kolouri, S., Rostami, M., Martin, C.E., Hoffmann, H., 2019. Explainability methods for graph convolutional neural networks. In: Proceedings of the IEEE/CVF Conference on Computer Vision and Pattern Recognition. pp. 10772–10781.

Qi, S., Meesters, S., Nicolay, K., ter Haar Romeny, B.M., Ossenblok, P., 2015. The influence of construction methodology on structural brain network measures: A review. J. Neurosci. Methods 253, 170–182.

Rusinek, H., De Santi, S., Frid, D., Tsui, W.-H., Tarshish, C.Y., Convit, A., de Leon, M.J., 2003. Regional brain atrophy rate predicts future cognitive decline: 6-year longitudinal MR imaging study of normal aging. Radiology 229 (3), 691–696.

Shchur, O., Mumme, M., Bojchevski, A., Günnemann, S., 2018. Pitfalls of graph neural network evaluation. arXiv preprint arXiv:1811.05868.

Soares, J.M., Marques, P., Alves, V., Sousa, N., 2013. A hitchhiker's guide to diffusion tensor imaging. Front. Neurosci. 7, 31.

Sotiropoulos, S.N., Zalesky, A., 2019. Building connectomes using diffusion MRI: why, how and but. NMR Biomed. 32 (4), e3752.

Sserwadda, A., Rekik, I., 2021. Topology-guided cyclic brain connectivity generation using geometric deep learning. J. Neurosci. Methods 353, 108988.

Tang, H., Guo, L., Fu, X., Qu, B., Thompson, P.M., Huang, H., Zhan, L., 2022a. Hierarchical brain embedding using explainable graph learning. In: 2022 IEEE 19th International Symposium on Biomedical Imaging. ISBI, IEEE, pp. 1–5.

Tang, H., Ma, G., Guo, L., Fu, X., Huang, H., Zhang, L., 2022b. Contrastive brain network learning via hierarchical signed graph pooling model. arXiv preprint arXiv:2207.07650.

Tang, H., Ma, G., He, L., Huang, H., Zhan, L., 2021. Commpool: An interpretable graph pooling framework for hierarchical graph representation learning. Neural Netw. 143, 669–677.

Tzourio-Mazoyer, N., Landeau, B., Papathanassiou, D., Crivello, F., Etard, O., Delcroix, N., Mazoyer, B., Joliot, M., 2002. Automated anatomical labeling of activations in SPM using a macroscopic anatomical parcellation of the MNI mri single-subject brain. Neuroimage 15 (1), 273–289.

Uludağ, K., Roebroeck, A., 2014. General overview on the merits of multimodal neuroimaging data fusion. Neuroimage 102, 3–10.

Van Essen, D.C., Smith, S.M., Barch, D.M., Behrens, T.E., Yacoub, E., Ugurbil, K., Consortium, W.-M.H., et al., 2013. The WU-minn human connectome project: an overview. Neuroimage 80, 62–79.

Veličković, P., Cucurull, G., Casanova, A., Romero, A., Lio, P., Bengio, Y., 2017. Graph attention networks. arXiv preprint arXiv:1710.10903.

Whitfield-Gabrieli, S., Nieto-Castanon, A., 2012. Conn: a functional connectivity toolbox for correlated and anticorrelated brain networks. Brain Connect. 2 (3), 125–141.

Wierenga, L.M., van den Heuvel, M.P., Van Dijk, S., Rijks, Y., de Reus, M.A., Durston, S., 2016. The development of brain network architecture. Human Brain Mapp. 37 (2), 717–729.

Yan, Y., Zhu, J., Duda, M., Solarz, E., Sripada, C., Koutra, D., 2019. Groupinn: Grouping-based interpretable neural network for classification of limited, noisy brain data. In: Proceedings of the 25th ACM SIGKDD International Conference on Knowledge Discovery & Data Mining. pp. 772–782.

Yeh, C.-H., Jones, D.K., Liang, X., Descoteaux, M., Connelly, A., 2021. Mapping structural connectivity using diffusion MRI: Challenges and opportunities. J. Magn. Reson. Imaging 53 (6), 1666–1682.

Ying, Z., You, J., Morris, C., Ren, X., Hamilton, W., Leskovec, J., 2018. Hierarchical graph representation learning with differentiable pooling. Adv. Neural Inf. Process. Syst. 31.

Zhan, L., Jenkins, L.M., Wolfson, O.E., GadElkarim, J.J., Nocito, K., Thompson, P.M., Ajilore, O.A., Chung, M.K., Leow, A.D., 2017. The significance of negative correlations in brain connectivity. J. Comp. Neurol. 525 (15), 3251–3265.

Zhan, L., Zhou, J., Wang, Y., Jin, Y., Jahanshad, N., Prasad, G., Nir, T.M., Leonardo, C.D., Ye, J., Thompson, P.M., et al., 2015. Comparison of nine tractography algorithms for detecting abnormal structural brain networks in Alzheimer's disease. Front. Aging Neurosci. 7, 48.

Zhang, Y., Huang, H., 2019. New graph-blind convolutional network for brain connectome data analysis. In: International Conference on Information Processing in Medical Imaging. Springer, pp. 669–681.

Zhang, L., Wang, L., Zhu, D., 2020a. Recovering brain structural connectivity from functional connectivity via multi-gcn based generative adversarial network. In: International Conference on Medical Image Computing and Computer-Assisted Intervention. Springer, pp. 53–61.

Zhang, L., Wang, L., Zhu, D., Initiative, A.D.N., et al., 2022. Predicting brain structural network using functional connectivity. Med. Image Anal. 79, 102463.

Zhang, W., Zhan, L., Thompson, P., Wang, Y., 2020b. Deep representation learning for multimodal brain networks. In: International Conference on Medical Image Computing and Computer-Assisted Intervention. Springer, pp. 613–624.

Zhang, Y., Zhan, L., Wu, S., Thompson, P., Huang, H., 2021. Disentangled and proportional representation learning for multi-view brain connectomes. In: International Conference on Medical Image Computing and Computer-Assisted Intervention. Springer, pp. 508–518.

Zhu, Q., Yang, J., Xu, B., Hou, Z., Sun, L., Zhang, D., 2021. Multimodal brain network jointly construction and fusion for diagnosis of epilepsy. Front. Neurosci. 1121.